Acta Materialia 307 (2026) 121969

Contents lists available at ScienceDirect

Acta Materialia

journal homepage: www.elsevier.com/locate/actamat

Full length article

Low Young's modulus achieved by anelastic relaxation arising from reversible atomic shuffling in bcc Ti–Nb alloys

Masakazu Tane [a,*], Keigo Morita [a], Eisuke Miyoshi [b], Takumi Hiramatsu [b]

[a] Division of Materials and Manufacturing Science, Graduate School of Engineering, The University of Osaka, 2-1 Yamadaoka, Suita, Osaka, 565-0871, Japan
[b] Graduate School of Engineering, Osaka Metropolitan University, 1-1 Gakuen-cho, Nakaku, Sakai, Osaka, 599-8531, Japan

ARTICLE INFO

Keywords:
Elastic properties
Relaxation
Titanium alloys
Phase transformation
Atomic shuffling

ABSTRACT

Metastable body-centered cubic (bcc) Ti alloys are attractive biomedical implant materials because they exhibit a low elastic modulus which helps mitigate bone degradation. The low elastic modulus in these alloys is believed to be correlated with a low-stability bcc structure. However, the physical nature of this correlation remains unclear. In this study, we show that the low elastic modulus of bcc Ti–Nb alloys originates from the anelastic relaxation driven by reversible atomic shuffling events that act as precursors to the ω (hexagonal) and α'' (orthorhombic) martensitic transformations. A combination of molecular-dynamics simulations and measurements of Young's modulus and internal friction revealed that the reversible atomic shuffling events have a low average activation energy of 0.20 eV, leading to significant anelastic relaxation even at room temperature (~300 K), thereby lowering the elastic modulus. The reversible atomic shuffling events occur in sub-nanometer-scale, low-stability bcc regions that are depleted in the bcc-stabilizing element Nb. These regions originate from quenched-in statistical compositional fluctuations, which exist even when the constitutive elements are randomly distributed. Thus, controlling the reversible atomic shuffling events by manipulating the compositional fluctuations and the resultant local chemical composition is an effective strategy for lowering the elastic modulus of biomedical bcc Ti alloys.

1. Introduction

A low elastic modulus is crucial for biomedical implant materials because it helps prevent bone degradation caused by the mismatch between the elastic moduli of the implant and natural bone [1–9]. Mg [10] and body-centered cubic (bcc, β-phase) Zr [11,12] alloys are considered candidates for biomedical implants due to their low elastic moduli. Metastable bcc Ti alloys are more attractive candidates for such implants because they exhibit low elastic moduli close to that of natural human bone, in addition to excellent biocompatibility, superior corrosion resistance, and high specific strength. To obtain a low Young's modulus in bcc Ti alloys, the formation of α'' (orthorhombic) martensite and the ω (hexagonal) phases, which have relatively high elastic moduli [13,14], should be suppressed, and a single bcc-phase state should be retained [15,16]. Furthermore, the elastic modulus of the bcc phase itself should be reduced. Previous studied indicate that the low elastic modulus of the bcc Ti alloys is correlated with a low-stability bcc structure [17–20]. However, the physical nature of this correlation has remained unclear for decades.

Metastable bcc Ti–Nb-based alloys (Ti–Nb and Ti–Nb–Ta–Zr alloys) with low-stability bcc structures exhibit a much lower Young's modulus than other Ti alloys [18,21,22], and also show excellent in vitro cytocompatibility (low cytotoxicity) and superior corrosion resistance [23,24], making them promising candidates for biomedical implant applications. These alloys exhibit a double softening of the single-crystal shear moduli: c' for $\{110\}\langle 1\bar{1}0\rangle$ shear and c_{44} for $\{100\}\langle 010\rangle$ shear, both of which contribute to the exceptionally low Young's modulus [21]. However, the underlying mechanisms for the softening of both c' and c_{44} remain unclear for both binary Ti–Nb and multicomponent Ti–Nb–Ta–Zr alloys [18,21,22]. The fact that this softening occurs in both systems suggests that the softening of c' and c_{44} is a general feature of Ti–Nb-based alloys with low-stability bcc structures, rather than a phenomenon limited to specific multicomponent systems. In the present work, we therefore focus on the binary Ti–Nb alloy as a model system. The simplicity of this binary system facilitates a clearer interpretation of the underlying mechanisms and enables a detailed analysis of the softening behavior of c' and c_{44} through molecular-dynamics (MD) simulations.

It has been proposed that the low Young's modulus in metastable bcc Ti alloys arises from a reduced stability of the bcc lattice near the martensitic transformation start (M_s) temperature, manifesting as significant lattice softening [5,25]. Specifically, bcc Ti–Nb alloys undergo

* Corresponding author.
E-mail address: tane@mat.eng.osaka-u.ac.jp (M. Tane).

https://doi.org/10.1016/j.actamat.2026.121969
Received 1 October 2025; Received in revised form 25 January 2026; Accepted 26 January 2026
Available online 27 January 2026

a phase transformation to the α'' (orthorhombic) martensite phase (Fig. 1(a) and 1(b)), accompanied by the softening of a short-wavelength transverse-acoustic $TA(1/2)(1,1,0)$ phonon with $[1\bar{1}0]$ polarization (Fig. 1(c) and 1(d)). This phonon softening is believed to be correlated with the reduction of c' [22]. However, the softening of short-wavelength phonons does not directly lead to a decrease in the shear modulus, because the shear modulus reflects the long-wavelength limit of acoustic phonons. To clarify this distinction, it is essential to consider the length scales associated with these lattice instabilities. The shear modulus c' is related to the initial slope of the transverse-acoustic phonon branch in the long-wavelength limit ($k \rightarrow 0$) near the Brillouin zone center (Γ point). This slope represents the macroscopic resistance of the bcc crystal to uniform $\{110\}\langle 1\bar{1}0\rangle$ shear deformation. In contrast, the softening of the $TA(1/2)(1,1,0)$ phonon corresponds to a reduced resistance against the microscopic shuffling of every other $\{110\}$ atomic plane. Similarly, the softening of a short-wavelength longitudinal acoustic $LA(2/3)(1,1,1)$ phonon, associated with the ω transformation (Fig. 2(a)–2(d)) [26,27], does not account for the reductions in c' and c_{44}. This fundamental problem is not unique to Ti alloys but is observed in other bcc-based materials [28–31]. In several bcc-based ordered compounds, the softening of c' is accompanied by a softening of short-wavelength transverse-acoustic phonons; however, the detailed correlation between these two phenomena remains unclear.

Recently, a new anelastic relaxation phenomenon associated with the ω transformation has been reported in bcc Ti–V-based alloys with low-stability bcc structures [32–34]. In these alloys, reversible atomic shuffling events (referred to as dynamic atomic shuffling in a previous paper [33]) that act as precursors to the ω-phase nucleation occur. This reversible shuffling occurs in locally less-stable bcc regions formed because of quenched-in statistical compositional fluctuations. According to thermodynamic fluctuation theory [35], in a solid solution containing more than two atomic species, the local atomic concentration fluctuates around its average value at sufficiently high temperatures where atomic diffusion occurs. When the alloy is quenched to room temperature, these compositional fluctuations are frozen in, producing a spatial variation in composition. This spatial variation is referred to as the quenched-in compositional fluctuation. The quenched-in compositional fluctuations are distinct from the compositional distributions formed via spinodal decomposition and are inevitably present in metallic materials, even when the constituent elements are randomly distributed. Therefore, the novel anelastic relaxation possibly affects the elastic properties of various bcc Ti alloys; however, its effect has not yet been clarified in previous studies [32,33]. Accordingly, we focus on analyzing the effect of anelastic relaxation on the low Young's modulus through MD simulations, combined with measurements of Young's modulus and internal friction. The binary Ti–Nb system is suitable for this study due to the availability of a reliable interatomic potential [36].

In this study, we investigate the origin of the low elastic modulus in bcc Ti–Nb alloys, focusing on the anelastic relaxation driven by pretransitional, reversible atomic shuffling events associated with the ω and α'' martensitic transformations. To analyze the effect of anelastic relaxation on the elastic properties at room temperature, the temperature dependences of Young's modulus and internal friction in a Ti–Nb polycrystal were measured from 300 K to 25 K (or 10 K). Although the elastic properties at low temperatures are not directly relevant to biomedical implant applications, understanding them helps clarify the elastic properties at room temperature. By analyzing the temperature dependence of internal friction, the activation energy for the reversible atomic shuffling was evaluated using the Debye model. MD simulations were conducted, and the elastic properties were analyzed using the stress-fluctuation formula to evaluate the anelastic contributions originating from the reversible atomic shuffling events. Moreover, the atomic displacement, displacement vector, relaxation time, and chemical compositions in the bcc regions that undergo reversible atomic shuffling were analyzed. A combination of the MD simulations and experimental measurements revealed that anelastic relaxation, driven by the reversible atomic shuffling events that act as precursors to the ω and α'' martensitic transformations, lowers the Young's modulus in bcc Ti–Nb alloys.

2. Methods

A Ti–28.6Nb(–0.3O)(at.%) alloy polycrystal was prepared from high-purity Ti and Nb by arc melting and subsequently homogenized at 1273 K for 3 days. The Ti and Nb concentrations were analyzed using an electron probe microanalyzer, and the oxygen content was determined using an oxygen analyzer. The oxygen content corresponds to an unavoidable impurity introduced during alloy preparation. Such a small amount of oxygen is not expected to significantly affect the activation energy for the anelastic relaxation process associated with atomic shuffling [33,40]. A plate specimen measuring $60.0 \times 6.0 \times 0.886$ mm^3 and a rectangular parallelepiped specimen measuring $4.08 \times 4.00 \times 3.11$ mm^3 were cut from the homogenized ingot for measuring the Young's modulus E and internal friction Q^{-1}. Both specimens were solution-treated at 1273 K for 1 h in vacuum and then quenched in ice water. No surface oxidation was observed on the quenched specimens. Furthermore, the residual stress induced by quenching was considered negligible due to the sufficiently small size of the specimens. The E and Q^{-1} values of the quenched plate specimens were measured from 300 K to 25 K in 5 K steps during cooling and subsequent heating via the cantilever resonance method (resonance frequency f_r = 166.4 Hz at 300 K). A cryogen-free system with the specimen in a static exchange-gas environment was used for the low-temperature measurements. During the measurements, the specimen was placed in a chamber filled with helium gas. After thermal equilibration within the chamber, the E and Q^{-1} of the specimen were measured. The temperature was monitored using a thermocouple placed near the specimen. Because the specimen was thermally equilibrated with the surrounding helium exchange gas, the specimen temperature was assumed to be equal to the gas temperature. The temperature dependence of Q^{-1} was measured using different resonance frequencies to analyze the activation energy of atomic relaxation using the Debye model. Q^{-1} of the quenched plate specimen was measured via the free vibration method (f_r = 854.2 Hz at 300 K). The Q^{-1} values of the quenched rectangular parallelepiped specimen were measured from 300 K to 10 K in 10 K steps via the free-decay method using an electromagnetic acoustic resonance method [41] with f_r = 433.7 kHz at 300 K. The peak temperature of Q^{-1} was determined by fitting the temperature-dependent Q^{-1} curves measured for three independent specimens. An Arrhenius plot was then constructed using the relationship between the peak temperature and the relaxation time obtained from these specimens. From this Arrhenius analysis, we determined the activation energy associated with the anelastic relaxation. Furthermore, the activation energy distribution was analyzed using the Debye model, assuming a Gaussian distribution. The observation of an internal-friction peak in all three specimens indicates that this peak is intrinsic to this alloy system; moreover, as described in the Results section, its peak temperature depends on the resonance frequency, demonstrating that the anelastic relaxation is a thermally activated process. For the measurement of Young's modulus using the cantilever resonance method, the resonance frequency was recorded with a step size of approximately 0.1–0.4 Hz, and the modulus was calculated from the resonance peak position. A frequency shift of 0.4 Hz corresponds to an uncertainty of approximately 0.03 GPa in Young's modulus.

MD simulations were performed using the LAMMPS code [42]. The simulation cell, which contained a total of 2000 atoms, was a $10 \times 10 \times 10$ supercell created by replicating the conventional two-atom bcc unit cell (space group $Im\bar{3}m$). Ti atoms were substituted for Nb to obtain Ti–xNb alloys with x ranging from 20 to 36 at.% in 1 at.% increments. The substitutional disorder was modeled using a

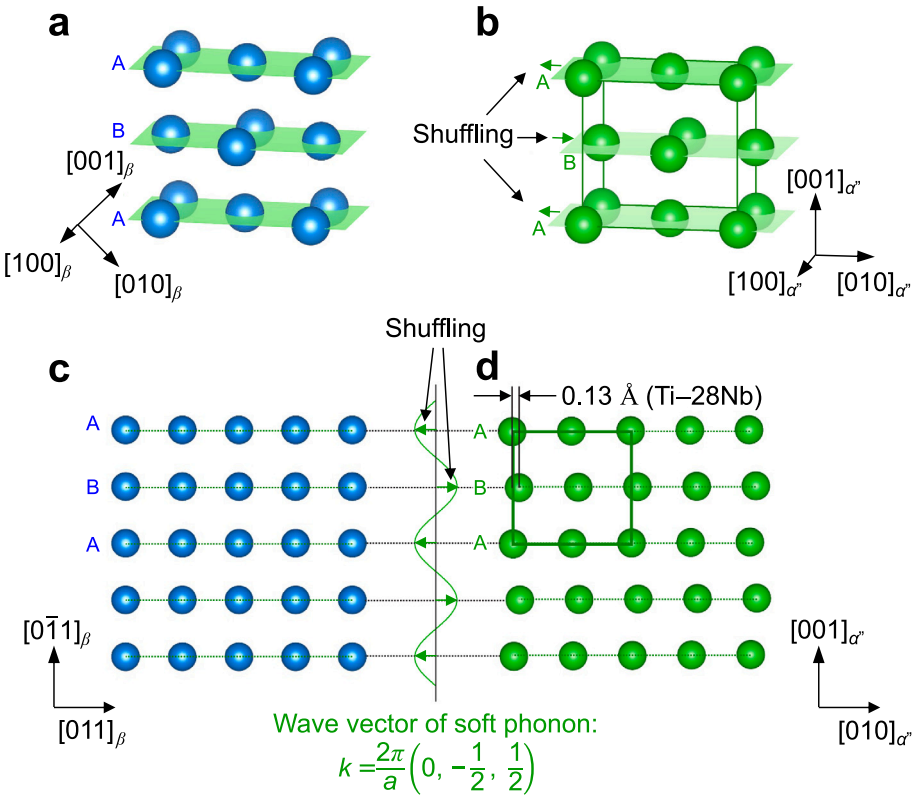

Fig. 1. Crystal structures of the (a) bcc (β) and (b) α'' martensite phases in Ti alloys, and atomic arrangements of the (c) bcc and (d) α'' phases viewed along the directions parallel to $[100]_\beta$ and $[100]_{\alpha''}$, respectively; the crystal structures were visualized with VESTA [37]. The shuffling of parallel adjacent $\{0\bar{1}1\}_\beta$ planes along the $\langle 011\rangle_\beta$ directions, indicated by the arrows, is necessary for the formation of the α'' martensite phase. This shuffling is associated with the phonon softening with the wave vector $\boldsymbol{k} = (2\pi/a)(0, -1/2, 1/2)$, where a is the lattice constant of the bcc phase. This phonon mode is called the $TA(1/2)(1,1,0)$ phonon. In addition to this atomic shuffling, the formation of α'' martensite requires macroscopic shear on the $\{112\}_\beta$ planes along the $\langle 11\bar{1}\rangle_\beta$ directions, whereas a nanodomain structure [38], also called the O′ phase [39], forms exclusively through atomic shuffling on the $\{0\bar{1}1\}_\beta$ planes.

special quasirandom structure generated by a Monte Carlo algorithm implemented in *mcsqs* within the ATAT package [43]. Atomic interactions were described by the force-matched empirical potential for Ti–Nb proposed by Ehemann and Wilkins [36]. Apart from accurately reproducing the lattice constants and cohesive energies of the bcc as well as the ω and α'' martensite phases predicted by density functional theory (DFT) calculations, the potential proposed therein also successfully predicts the α'' martensitic transformation strain. In addition, the single-crystal elastic constants computed using the force-matched empirical potential are consistent with available experimental data as well as with DFT calculations [36]. Although the full phonon dispersion curves, including α'' martensitic transformation, were not checked, the phonon mode that governs the ω transformation was validated. Specifically, the potential was refined to reproduce the $LA(2/3)(1,1,1)$ mode, and it captures the DFT-predicted energy barrier associated with the atomic shuffles along the $\omega \leftrightarrow \beta$ transformation pathway corresponding to this phonon mode.

The supercell was first equilibrated in the isothermal–isobaric (NPT) ensemble at 300 K and zero pressure for 300 ps with a 1 fs time step. The temperature and pressure were controlled using a Nosé–Hoover chain thermostat-barostat, and periodic boundary conditions were applied in all three directions. For Ti–28Nb and Ti–33Nb, the temperature was then varied to 10, 25, 50, 75, 100, 125, 150, 200, 250, 300, 400, 500, and 600 K at a cooling or heating rate of 10 K ps^{-1} in the NPT ensemble, followed by a 200 ps equilibration at each temperature. Finally, the elastic-stiffness tensor was calculated at every temperature in simulations with a constant number of atoms, constant volume, and constant temperature (NVT). The elastic-stiffness tensor for Ti–25Nb was calculated over 260–300 K in 5 K increments, and that for the Ti–Nb alloys except Ti–25Nb, Ti–28Nb, and Ti–33Nb was calculated at 300 K.

The stress-fluctuation formula was used to examine the effect of anelastic relaxation on the elastic properties. The elastic stiffness tensor C_{ijkl} at finite temperature T is given by [44,45]:

$$C_{ijkl} = \langle C^{\mathrm{B}}_{ijkl}\rangle - \frac{V}{k_{\mathrm{B}}T}(\langle\sigma_{ij}\sigma_{kl}\rangle - \langle\sigma_{ij}\rangle\langle\sigma_{kl}\rangle) + \frac{2Nk_{\mathrm{B}}T}{V}(\delta_{il}\delta_{jk} + \delta_{ik}\delta_{jl}), \quad (1)$$

where σ_{ij} is the stress tensor, V is the volume containing the N (= 2000) atoms, δ_{ij} is the Kronecker delta, k_{B} is the Boltzmann constant, and $\langle\cdot\rangle$ denotes an ensemble average. The term $\langle C^{\mathrm{B}}_{ijkl}\rangle = (1/V)(\partial^2 U/(\partial\epsilon_{ij}\partial\epsilon_{kl}))$ corresponds to the Born contribution: the instantaneous affine response obtained when all atoms follow the imposed macroscopic strain without relaxation; U and ϵ_{ij} denote the potential energy and strain tensor, respectively. The second term $C^{\mathrm{F}}_{ijkl} = -\{V/(k_{\mathrm{B}}T)\}(\langle\sigma_{ij}\sigma_{kl}\rangle - \langle\sigma_{ij}\rangle\langle\sigma_{kl}\rangle)$ is the stress-fluctuation contribution and reflects the non-affine response leading to stress relaxation. The third term is the kinetic (ideal-gas) contribution, which originates from thermal momentum fluctuations. The Born term and stress tensor components were calculated at 1-fs intervals, and their ensemble averages were accumulated over 1 ns. The elastic-stiffness tensor C_{ijkl} was then computed from these averages. Eq. (1) is based on the stress-fluctuation formalism, in which the isothermal elastic stiffness tensor is obtained from equilibrium stress fluctuations at fixed temperature and fixed simulation cell shape (i.e., in the NVT ensemble; $N = 2000$). Therefore, no finite deformation steps are required to evaluate C_{ijkl}, in contrast to a finite-strain stress–strain method. Importantly, when thermally

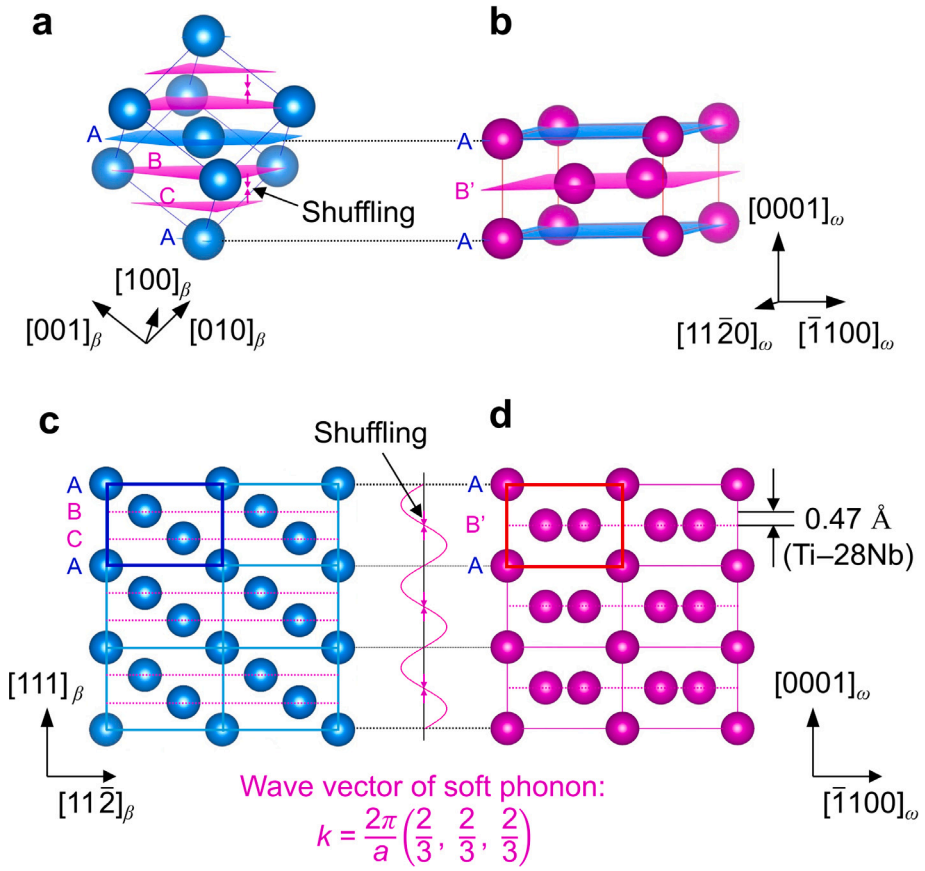

Fig. 2. Crystal structures of the (a) bcc (β) and (b) ω phases in Ti alloys, and atomic arrangements of the (c) bcc and (d) ω phases viewed along the directions parallel to $[1\bar{1}0]_\beta$ and $[11\bar{2}0]_\omega$, respectively; the crystal structures were visualized with VESTA [37]. Atomic shuffling, that is, the collapse of $\{111\}_\beta$ lattice plane pairs (indicated by the arrows) is necessary for the formation of the ω phase. This atomic shuffling is associated with the phonon softening with the wave vector $\boldsymbol{k} = (2\pi/a)(2/3, 2/3, 2/3)$, where a is the lattice constant of the bcc phase. This phonon mode is called the $LA(2/3)(1, 1, 1)$ phonon.

activated atomic movements occur during the NVT simulation, the stress tensor exhibits enhanced fluctuations. As a result, the stress-covariance (fluctuation) contribution in Eq. (1) is finite and reduces the isothermal elastic stiffness. The fluctuation term therefore quantifies the extent to which thermally activated local, non-affine relaxations soften the elastic response relative to the purely affine (Born) contribution. The polycrystalline Young's modulus E was calculated from the C_{ijkl} components using the Voigt–Reuss–Hill approximation [46].

The atomic relaxation underlying the anelastic response was investigated by evaluating the magnitudes and orientations of atomic displacement vectors within the same NVT ensemble used in the elastic-stiffness tensor calculations. We also calculated the intermediate scattering function in the NVT ensemble to evaluate the activation energy H_a associated with the atomic relaxation:

$$F(\boldsymbol{q}, t) = \frac{1}{N}\sum_{i=1}^{N}\sum_{j=1}^{N}\left\langle e^{i\boldsymbol{q}\cdot(\boldsymbol{r}_i(t)-\boldsymbol{r}_j(0))}\right\rangle, \tag{2}$$

where N is the number of atoms, $\boldsymbol{q}$ is the wave vector, and $\boldsymbol{r}_i(t)$ is the position of atom i at time t. The activation energy H_a was evaluated based on the assumption that the relaxation process is thermally activated and follows Arrhenius behavior. We assumed that the relaxation time τ, determined from the intermediate scattering function, is inversely proportional to the activation rate of atomic relaxation. We further assumed that the time constant τ_0 is temperature-independent over the temperature range examined, which allowed H_a to be evaluated from the Arrhenius relation:

$$\ln\tau = \ln\tau_0 + \frac{H_a}{k_B T}. \tag{3}$$

Because the total MD sampling time is 1 ns, the MD simulations reflect elastic properties influenced by anelastic relaxation processes with activation frequencies up to ~1 GHz. On the other hand, the measured Young's modulus reflects anelastic relaxation in the ~0.2–400 kHz range, corresponding to the resonance frequencies used in the experiments. Nevertheless, the simulation and experimental results can be compared by focusing on the temperature dependence of the elastic response associated with anelastic relaxation. This is because changing the observation frequency shifts the freezing temperature of the atomic relaxation, without altering the qualitative temperature dependence of the elastic properties, when the anelastic relaxation is governed by thermally activated atomic movements. Furthermore, the activation frequencies can be compared by evaluating the activation energy for atomic relaxation from the intermediate scattering function in the MD simulations and from internal friction in the experiments.

3. Results

3.1. Anomalous temperature dependence of Young's modulus and its correlation with thermally activated atomic relaxation

The Young's modulus of a Ti–28.6Nb (at.%) alloy polycrystal exhibited an anomalous temperature dependence. Fig. 3 presents the experimentally measured polycrystalline (a) Young's modulus E and (b) internal friction Q^{-1} of Ti–28.6Nb during cooling and heating as a function of temperature. The temperature dependences of Young's modulus and internal friction exhibited negligible thermal hysteresis between cooling and heating, indicating that the α'' martensitic transformation (nucleation of α'' phase) did not occur even upon cooling

to low temperatures. As shown in Fig. 3(a), the Young's modulus decreased upon cooling from 300 K, reached a minimum at approximately 155 K, and increased sharply thereafter with further cooling. A large peak in the internal friction Q^{-1} was observed near the onset of this sharp increase (around 100 K), as shown in Fig. 3(b).

Fig. 3(c) shows the temperature dependence of internal friction Q^{-1} in the Ti–28.6Nb alloy, measured by cantilever resonance (CR), free vibration (FV), and electromagnetic acoustic resonance (EMAR), with resonance frequencies f_r of 166.4 Hz for CR, 854.2 Hz for FV, and 433.7 kHz for EMAR. The peak temperature of Q^{-1} was lowest for CR and highest for EMAR, indicating that it shifted to higher values with an increase in the resonance frequency f_r.

Fig. 3(d) shows the Arrhenius plots of relaxation time τ associated with the atomic relaxation responsible for the internal-friction peak. The τ values were determined by analyzing the internal-friction peaks using the Debye model [47]. An approximately linear relationship was observed between $\ln\tau$ and $1/T$. Linear fitting of the Arrhenius plots yielded an activation energy $H_a = 0.21$ eV and a pre-exponential time constant $\tau_0 = 1.4 \times 10^{-14}$ s.

In the Debye relaxation model, we assumed a Gaussian distribution of the activation energy [48] to account for the effect of quenched-in compositional fluctuations on the activation-energy distribution. Under this assumption, the temperature dependence of internal friction $Q^{-1}(T)$ is given by

$$Q^{-1}(T) = \frac{\Delta_M}{2}\int_0^\infty \frac{1}{\sqrt{2\pi\sigma_a^2}}\exp\left[-\frac{\left(H_a-\overline{H}_a\right)^2}{2\sigma_a^2}\right]\times \operatorname{sech}\left[\frac{H_a}{k_B T}+\ln(\omega_r\tau_0)\right] dH_a, \quad (4)$$

where $\omega_r(=2\pi f_r)$ is the angular frequency, and $\overline{H}_a$ and σ_a are the average and standard deviations of the activation energy, respectively. The relaxation strength Δ_M and pre-exponential time constant τ_0 (1.4×10^{-14} s) were assumed to be constant values. By the fitting of Eq. (4) to the experimental data, the probability distribution of activation energy H_a was determined. The average $\overline{H}_a$ and standard deviation σ_a are 0.20 eV and 0.035 eV, respectively. The fitted curve, along with the measured internal friction data, is shown in Supplementary Fig. S1. Fig. 3(e) presents the probability distribution of H_a. The activation energy H_a exhibits a broad distribution, which is probably attributable to quenched-in compositional fluctuations. The relaxation frequency f_a, calculated from $\overline{H}_a$ and τ_0 via $f_a = 1/(2\pi\tau)$, decreased sharply at temperatures below 100 K, as shown in Fig. 3(f). This indicates that the sharp increase in Young's modulus below ~100 K results from the freezing of atomic relaxation, a phenomenon known as the ΔM effect [47].

3.2. Effect of stress relaxation on the softening in elastic moduli

The MD simulations using the stress-fluctuation formula reproduced the experimentally observed anomalous temperature dependence of Young's modulus. Fig. 4(a) shows the temperature dependence of the calculated polycrystalline Young's modulus E for the Ti–28Nb and Ti–33Nb alloys. For Ti–33Nb, E decreased upon cooling from 600 K, reached a minimum at 100 K, and increased sharply at lower temperatures. These calculated results were in good agreement with the experimental observations. For Ti–28Nb, wherein the stability of the bcc structure is lower than that of the Ti–33Nb bcc structure, although the temperature dependence of E was similar to that of Ti–33Nb, the E values were lower than those of Ti–33Nb above 100 K. This trend is consistent with those reported in previous studies: a reduction in the bcc stability due to a lower concentration of bcc-stabilizing elements leads to a lower Young's modulus [17,18]. Although the calculated temperature dependence of Young's modulus is qualitatively consistent with the experimental trend, small quantitative deviations remain. Above 150 K the measured Young's modulus exhibits a nearly linear decrease with increasing temperature (Fig. 3(a)), whereas the MD results show a more pronounced nonlinear concave-down (upward-convex) dependence (Fig. 4(a)). This discrepancy possibly reflects the limited transferability of the empirical potential used in this study.

For both Ti–28Nb and Ti–33Nb, the single-crystal shear modulus c' decreased upon cooling from 600 K, reached a minimum, and increased thereafter with a further decrease in the temperature, as shown in Fig. 4(b). The c' value of Ti–28Nb, which has a less-stable bcc phase, was lower than that of Ti–33Nb at $T \geq 100$ K. The temperature-dependence of the single-crystal shear modulus c_{44} was similar to that of c' (Supplementary Fig. S2(a)), whereas the bulk modulus B remained largely constant over the entire temperature range (Supplementary Fig. S2(d)). These results indicate that the anomalous temperature dependences of c' and c_{44} lead to the corresponding anomalous dependence of the polycrystalline Young's modulus E. Moreover, for the Ti–25.6Nb single crystal [22], the experimentally measured c' and c_{44} decreased upon cooling from 300 K, consistent with the calculated trends (Supplementary Figs. S3(a) and S3(b)). Furthermore, at 300 K, the calculated single-crystal moduli c', c_{44}, and B, as well as the polycrystalline Young's modulus E, were in good agreement with their experimental values (Supplementary Figs. S4(a), S4(d), S5(a), and S5(d)). These results validate the stress-fluctuation formula used to evaluate the elastic properties of Ti–Nb alloys.

The origin of the anomalous temperature dependences of c' and c_{44} was examined by separating the corresponding Born and stress-fluctuation contributions using the stress-fluctuation formula. As shown in Fig. 4(c) the Born contribution to c' increased with a decrease in the temperature for both Ti–28Nb and Ti–33Nb. This indicates that c' does not soften upon cooling under affine deformation (i.e., without atomic relaxation). In contrast, the stress-fluctuation contribution, reflecting non-affine atomic relaxation, decreased upon cooling from 600 K and reached a minimum near 100 K, similar to that in the case of c'. A similar temperature dependence was observed for the stress-fluctuation contribution to c_{44} (Supplementary Fig. S2(c)), whereas the corresponding Born contribution decreased only marginally upon cooling (Supplementary Fig. S2(b)). These large stress-fluctuation contributions to c' and c_{44} at low temperatures are consistent with the appearance of the internal friction peak at low temperatures, as both phenomena originate from stress relaxation due to atomic relaxation. Consequently, these results indicate that the anomalous temperature dependences of c' and c_{44} originate from stress relaxation.

3.3. Origin of atomic relaxation responsible for large stress relaxation

The element-resolved atomic displacements were analyzed to identify the element that contributes to a greater extent to the atomic relaxation that leads to large stress fluctuations (i.e., large stress relaxation). Fig. 5(a) shows the temperature dependence of the average displacements of Ti and Nb atoms from their equilibrium positions, d_{Ti} and d_{Nb}, in the NVT ensemble simulation for the Ti–28Nb alloy. The displacements of Ti atoms were greater than those of Nb atoms at all examined temperatures, indicating that the positional fluctuations for Ti atoms are larger than those for Nb atoms. From these average displacements, the ratio of the average displacement of Ti atoms to that of Nb atoms, d_{Ti}/d_{Nb}, was calculated (Fig. 5(b)). The ratio d_{Ti}/d_{Nb} reached its maximum around 150–200 K, the temperature range at which the stress fluctuations are significant (Fig. 4(d)). This implies that the Ti-atom fluctuations contribute to stress relaxation to a greater extent than Nb-atom fluctuations. This is consistent with the results reported in previous studies which suggest that atomic relaxation occurs preferentially in locally less-stable, Ti-rich regions formed by quenched-in statistical compositional fluctuations [32,33].

The origin of atomic fluctuations was examined by analyzing their correlation with the local Nb concentration in the sub-nanoscale regions. Supplementary Fig. S6 shows the local Nb concentration c_{Nb}

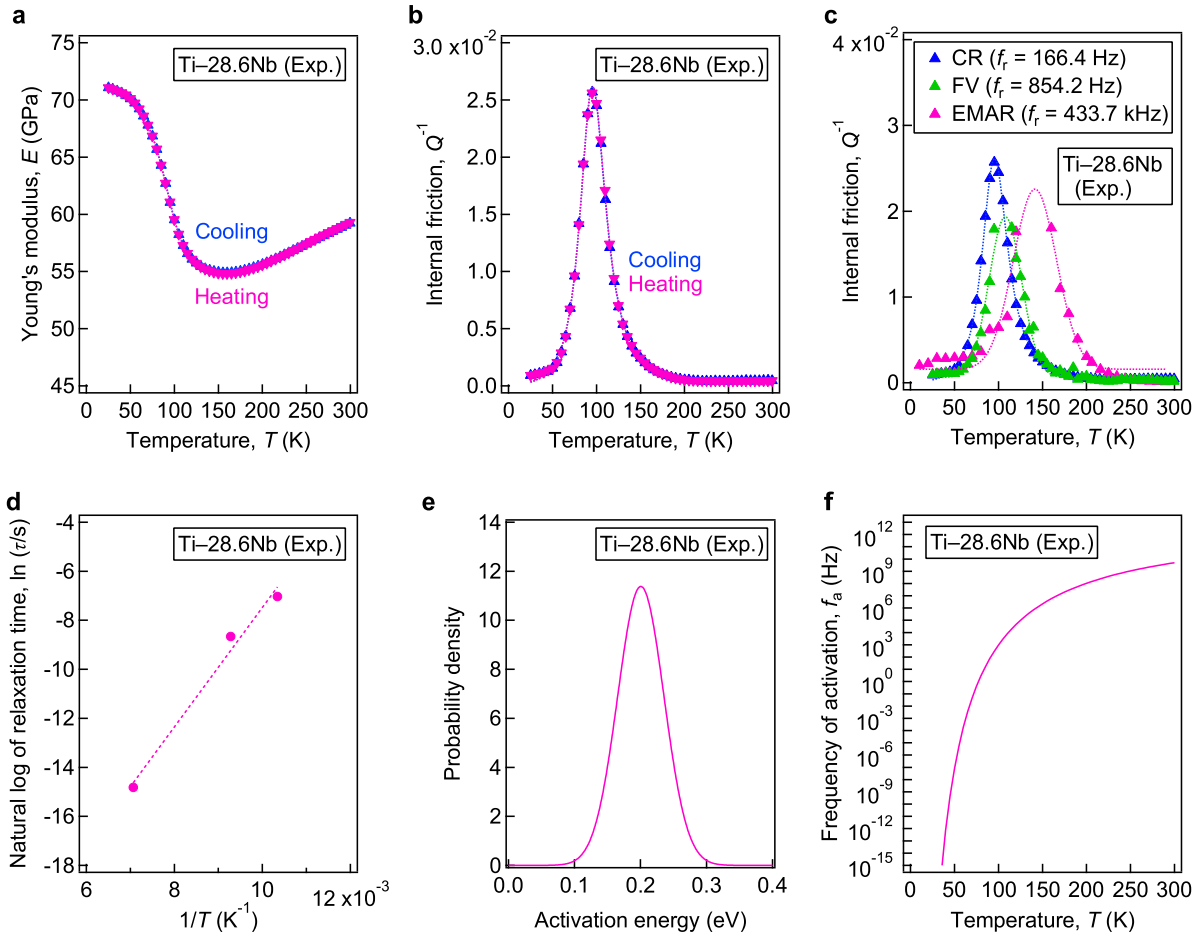

Fig. 3. Results of the experimental analyses of elastic properties and atomic relaxation. Temperature dependence of the (a) polycrystalline Young's modulus E and (b) internal friction Q^{-1} for the Ti–28.6Nb alloy during cooling and heating, measured via the cantilever resonance method. (c) Temperature dependence of internal friction Q^{-1} in the Ti–28.6Nb alloy, measured via the cantilever resonance (CR), free vibration (FV), and electromagnetic acoustic resonance (EMAR) methods. (d) Arrhenius plot of the relaxation time τ associated with the atomic relaxation responsible for the internal-friction peak, analyzed using the Debye model. (e) Probability distribution of the activation energy H_a determined from the temperature dependence of internal friction measured by CR. (f) Frequency of activation f_a for atomic relaxation leading to internal-friction peaks.

within the second-nearest-neighbor (2NN) shell (a sphere of radius $r \leq 4.0$ Å) in the NVT ensemble simulation for the Ti–28Nb alloy at 150 K; this 2NN shell contains 15 atoms. The Nb concentration c_{Nb} fluctuates statistically within this shell even for a quasirandom distribution of Ti and Nb atoms, arising from quenched-in statistical compositional fluctuations [32,33]. Fig. 6(a) shows the average displacement of constituent atoms from their equilibrium positions as a function of the local Nb concentration c_{Nb} within the 2NN shell. The average displacement and the standard deviation increased with a decrease in c_{Nb}. This indicates that large atomic fluctuations occur predominantly in Nb-lean regions wherein the local stability of the bcc lattice is lower. Fig. 6(b) shows the correlation coefficient R between the average atomic displacement and local Nb concentration c_{Nb} within spheres of different radii r. The selected radii, r = 3.1, 4.0, 5.0, 6.1, 6.8, and 7.7 Å, correspond to the 1st through the 6th neighbor shells, respectively. For $r \leq 4.0$ Å (i.e., within the 2NN shell), R approaches −1, indicating a very strong inverse correlation. The correlation is weaker for other radii. These results indicate that the local Nb concentration within the 2NN shell is the primary factor governing the magnitude of atomic fluctuations. This interaction range is significantly shorter than the dimensions of our 10 × 10 × 10 supercell (approximately 32.8 Å in length). Therefore, the 2000-atom model is sufficiently large to capture the compositional fluctuations responsible for the observed atomic fluctuations. Furthermore, the correlation coefficient in Fig. 6(b), calculated using the local Nb concentration and displacement data from all 2000 atomic sites, is based on an ensemble of diverse local environments that is statistically sufficient to validate the identified relationship.

The crystallographic orientations of atomic fluctuations of the Ti–28Nb alloy were analyzed to examine their correlation with pretransitional atomic shuffling. Fig. 7(a) shows a stereographic projection of the maximum atomic-displacement vectors observed at 600 K in an NVT simulation. The large displacement vectors were distributed almost isotropically over all crystallographic directions. In contrast, at 150 K, the distribution of the large displacement vectors was highly anisotropic, as shown in Fig. 7(b). Fig. 7(d) shows the weighted density map of the maximum atomic displacements at 150 K, calculated for vectors with magnitudes ≥ 0.7 Å. The density mapping indicates that the large-amplitude vectors were aligned predominantly near the ⟨111⟩ and ⟨101⟩ directions and were absent near the ⟨001⟩ directions. However, the distribution of large displacement vectors turned more isotropic again at 75 K, as shown in Fig. 7(c). These results indicate that large atomic fluctuations have preferential orientations at 150 K, at which stress fluctuations are significant (Fig. 4(d)). These preferred directions, ⟨111⟩ and ⟨101⟩, correspond to the atomic-shuffling directions involved in the ω and α'' martensitic transformations, respectively (Figs. 1 and 2). The ω transformation requires atomic shuffling of approximately 0.47 Å along ⟨111⟩. The large displacement amplitudes observed at 150 K exceed the magnitude of atomic shuffling required for the ω transformation. The α'' martensitic transformation requires an estimated

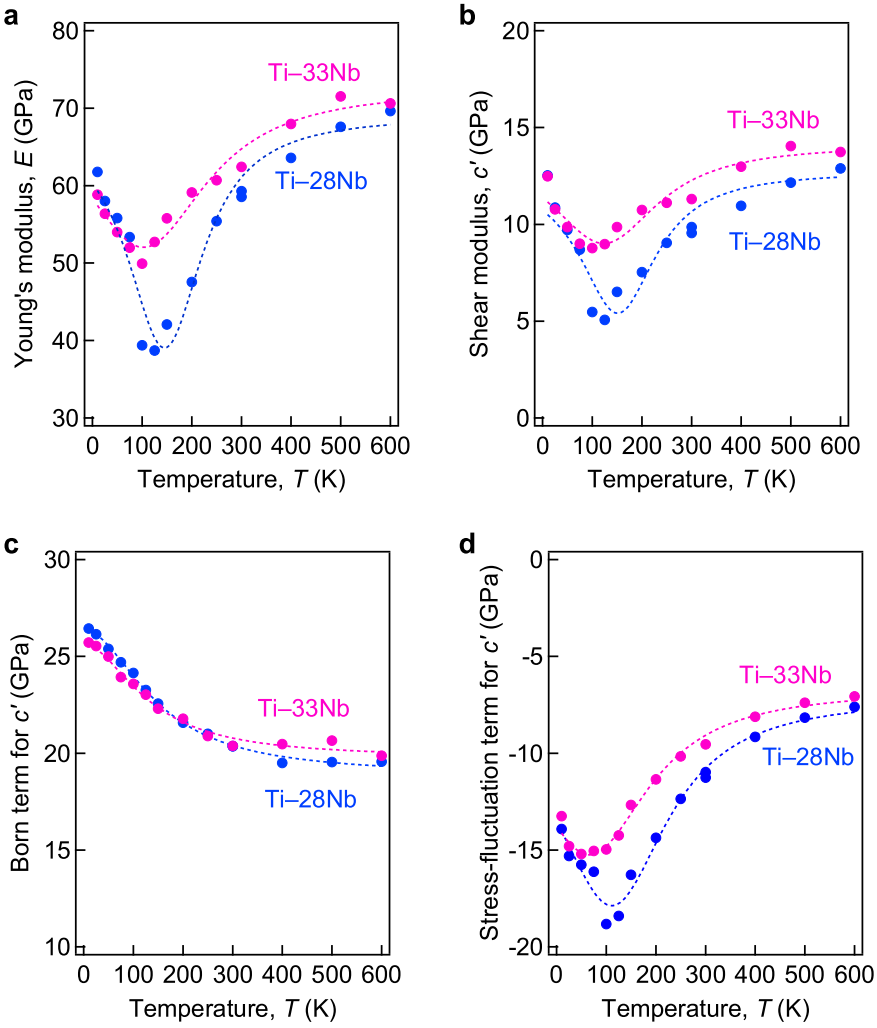

Fig. 4. Results of analysis of stress-relaxation effects on the elastic properties using MD simulations. Temperature dependence of the (a) polycrystalline Young's modulus E and (b) single-crystal shear modulus c' for the Ti–28Nb and Ti–33Nb alloys, calculated using the stress-fluctuation formula and Voigt–Reuss–Hill approximation. (c) Born-term and (d) stress-fluctuation-term contributions to the single-crystal shear modulus c' in Ti–28Nb and Ti–33Nb alloys, calculated using the stress-fluctuation formula.

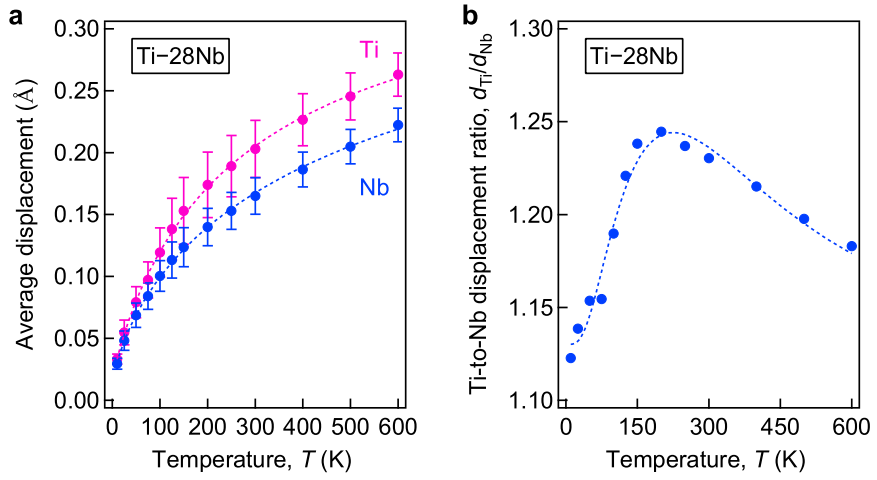

Fig. 5. Results of analysis of element-resolved atomic displacements. (a) Temperature dependence of the average displacements of Ti and Nb atoms from their equilibrium positions, d_{Ti} and d_{Nb}, in an NVT ensemble simulation for Ti–28Nb. (b) Ratio of the average displacement of Ti atoms to that of Nb atoms (d_{Ti}/d_{Nb}) in Ti–28Nb, calculated by averaging the absolute displacements from their time-averaged equilibrium positions during the NVT ensemble simulation.

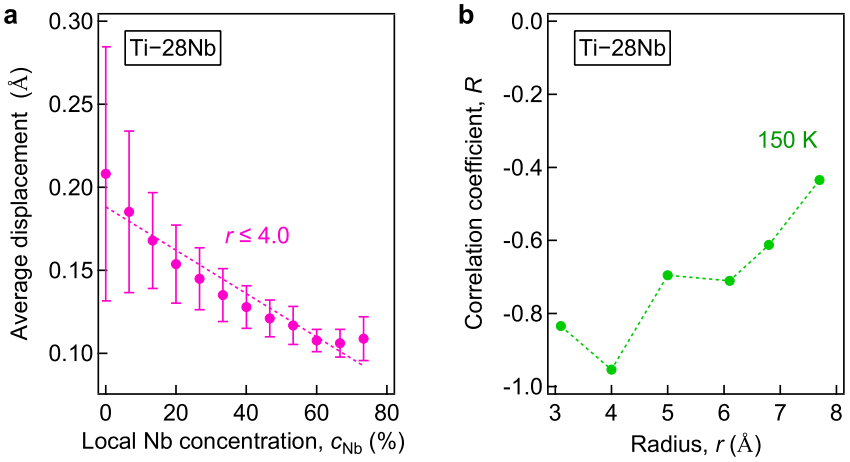

Fig. 6. Atomic fluctuations responsible for stress relaxation. (a) Average displacement of constituent atoms from their equilibrium positions as a function of the local Nb concentration c_{Nb} within the second-nearest-neighbor shell in the NVT simulation for Ti–28Nb at 150 K. (b) Correlation coefficient R between the average atomic displacement and local Nb concentration c_{Nb} in spherical regions with a radii r in the NVT ensemble simulation for Ti–28Nb at 150 K.

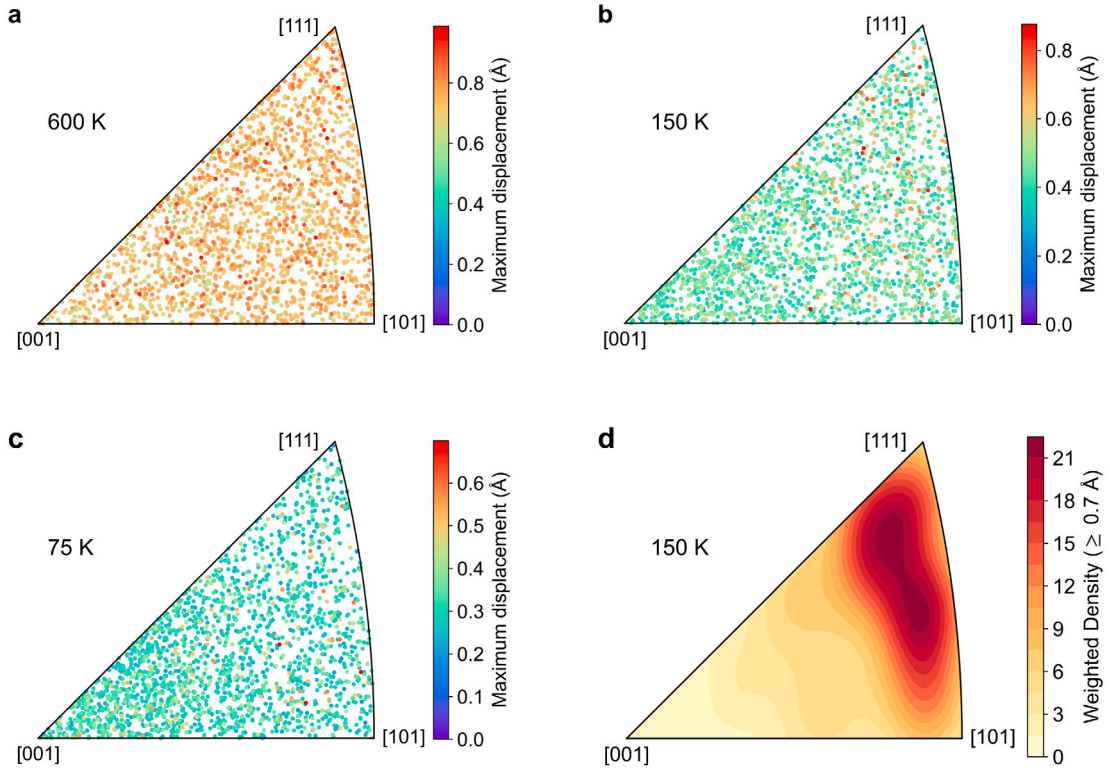

Fig. 7. Stereographic projections of the maximum atomic-displacement vectors observed in NVT MD simulations for Ti–28Nb at (a) 600, (b) 150, and (c) 75 K. (d) Weighted density map of the maximum atomic displacements at 150 K, calculated for vectors with magnitudes ≥ 0.7 Å.

atomic shuffling of 0.13 Å along ⟨101⟩ in Ti–28Nb [49], which is considerably smaller than that required for the ω transformation. Consistent with this difference, the large-amplitude displacement vectors tend to be located around ⟨111⟩ rather than ⟨101⟩ (Fig. 7(b) and 7(d)). These results indicate that the observed atomic fluctuations originate from the shuffling events associated with the ω and α'' transformations.

3.4. Thermal activation of pretransitional, reversible atomic shuffling events

The formation of α'' martensite requires macroscopic lattice shear in addition to atomic shuffling. In contrast, a nanodomain structure [38], also referred to as the O′ phase [39], forms exclusively via atomic shuffling on the $\{0\bar{1}1\}_\beta$ planes, which is associated with the α'' martensitic transformation (Fig. 1(c) and 1(d)). The ω phase is also formed predominantly via the collapse of $\{111\}_\beta$ plane pairs resulting from atomic shuffling. Therefore, the atomic shuffling behavior can be examined by analyzing the formation of the nanodomain structure and ω phase. Accordingly, we analyzed their formation behaviors by evaluating the corresponding static structure factors $S(\boldsymbol{q})$ that are the intermediate scattering functions $F(\boldsymbol{q}, t)$ at $t = 0$. Fig. 8(a) shows $S(\boldsymbol{q})$ as a function of the wave-vector magnitude ξ along the $[\xi, \xi, \xi]$ direction in Ti–28Nb. The plotted $S(\boldsymbol{q})$ values are averaged over crystallographically equivalent wave vectors and a is the lattice constant of the bcc structure. At 75 and 150 K, a small peak appeared at $\boldsymbol{q} \approx (2\pi/a)(4/3, 4/3, 4/3)$, indicating that a small fraction of the ω phase is formed at these low

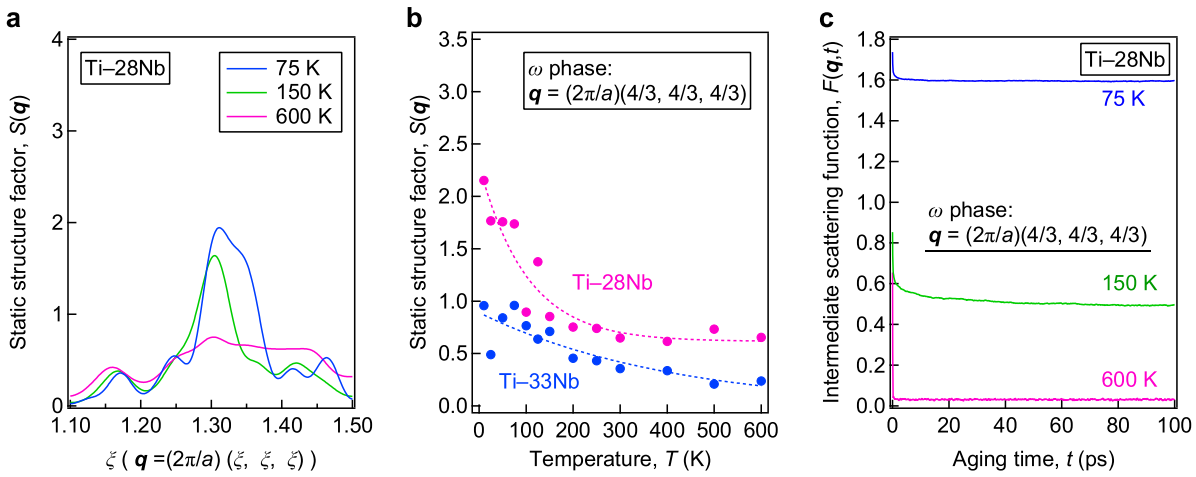

Fig. 8. Correlation between atomic shuffling and phase transformations. (a) Static structure factor $S(\boldsymbol{q})$ plotted against the wave-vector magnitude ξ along the $[\xi,\xi,\xi]$ direction in NVT ensemble simulations for Ti–28Nb at 75, 150, and 600 K. (b) Static structure factor $S(\boldsymbol{q})$ for the ω phase ($\boldsymbol{q} = (2\pi/a)(4/3,4/3,4/3)$) in NVT ensemble simulations for Ti–28Nb and Ti–33Nb alloys as a function of temperature. (c) Intermediate scattering function $F(\boldsymbol{q},t)$ for the ω phase as a function of the aging time t in NVT ensemble simulations for the Ti–28Nb alloy at 75, 150, and 600 K. $S(\boldsymbol{q})$ and $F(\boldsymbol{q},t)$ values were averaged over crystallographically equivalent wave vectors.

temperatures. This assignment is based on the crystallographic correspondence that the wave vector $\boldsymbol{q} \approx (2\pi/a)(4/3,\ 4/3,\ 4/3)$, expressed in the bcc reciprocal lattice, corresponds to the ω-phase $(0002)_\omega$ reciprocal lattice point [50]. Consequently, in our MD-based static structure factor analysis, this $\boldsymbol{q}$ reflects the density correlations associated with the structural periodicity along the $\langle 111\rangle_\beta \parallel [0001]_\omega$ direction. For Ti–28Nb, the intensity of this peak increased with a decrease in the temperature (Fig. 8(b)) and was higher than that for Ti–33Nb at all temperatures examined. These results are consistent with the fact that the stability of the ω phase increases with a decrease in the temperature and fraction of the bcc-stabilizing element [26]. The nanodomain (O′) structure was also formed at low temperatures (Supplementary Figs. S7(a) and S7(b)). These results indicate the occurrence of pretransitional, atomic shuffling events, which lead to the formation of the ω phase and nanodomain (O′) structure at low temperatures.

We analyzed the stabilities of the ω phase and nanodomain structure by evaluating the intermediate scattering function, $F(\boldsymbol{q},t)$. Fig. 8(c) shows $F(\boldsymbol{q},t)$ for the Ti–28Nb alloy as a function of the aging time t at 75, 150, and 600 K. The wave vector $\boldsymbol{q} = (2\pi/a)(4/3,4/3,4/3)$ corresponds to the formation of the ω-phase. At 75 K, initially, $F(\boldsymbol{q},t)$ decreased sharply at $t \approx 0$ owing to phonon vibrations, after which it remained largely constant. This indicates that the formed ω phase is stable and atomic relaxation on the simulation timescale is negligible. However, at 150 K, after the initial phonon-induced decrease, $F(\boldsymbol{q},t)$ decreased gradually without reaching zero. This indicates that a portion of the ω structure is unstable and reverts to the bcc phase via atomic relaxation. In other words, a portion of the formed ω structure is embryonic and does not achieve stable nucleation. At the higher temperature of 600 K, $F(\boldsymbol{q},t)$ decreased to nearly zero almost immediately ($t \approx 0$), indicating that the formed embryonic ω structure is highly unstable and reverts immediately to the bcc structure. A similar analysis for the nanodomain (O′) structure, using $\boldsymbol{q} = (2\pi/a)(1/2,0,3/2)$, revealed that the temperature dependence of the atomic relaxation process was similar to that for the ω phase (Supplementary Fig. S7(c)). These results indicate that the relaxation process is strongly temperature-dependent. In addition to the aforementioned reverse relaxation (from ω or nanodomain to bcc), a forward relaxation (from bcc to ω or nanodomain) is also expected. However, this forward process could not be quantitatively analyzed because the change in $F(\boldsymbol{q},t)$ for the bcc structure was negligible compared to its initial value, $F(\boldsymbol{q},0)$. These findings suggest that reversible atomic shuffling events, including the forward and reverse atomic relaxation processes, occur and that the relaxation time strongly depends on temperature.

The activation energy for the reverse atomic relaxation (from ω or nanodomain to bcc) was analyzed to examine its correlation with the experimentally observed anelastic relaxation. Fig. 9(a) shows Arrhenius plots of the relaxation time τ determined from the intermediate scattering function $F(\boldsymbol{q},t)$. The plots correspond to the relaxation from the ω phase ($\boldsymbol{q} = (2\pi/a)(4/3,4/3,4/3)$) and the nanodomain structure ($\boldsymbol{q} = (2\pi/a)(1/2,0,3/2)$) to the bcc structure. The relationships between $\ln\tau$ and $1/T$ were approximately linear for both relaxation processes. Linear fits to the plots yielded an activation energy $H_a = 0.084$ eV and a pre-exponential factor $\tau_0 = 1.3 \times 10^{-14}$ s for the relaxation from the ω phase. The corresponding values for the relaxation from the nanodomain structure were 0.083 eV and 2.6×10^{-14} s, respectively. The activation energies obtained from the MD simulations (0.083–0.084 eV) were smaller than the experimental values determined via the internal-friction experiments (average value of 0.20 eV). This discrepancy is probably attributed to differences in the relaxation processes evaluated by each method. The occurrence of reverse relaxation (from the ω phase or nanodomains to bcc) indicates that the embryonic ω or nanodomain structures are less stable than the bcc structure. This suggests that the activation barriers for the forward and reverse atomic relaxation processes are asymmetric, with the forward barrier potentially exceeding the reverse one, as shown in Fig. 9(c). Similar forward–reverse barrier asymmetry has been reported for relaxation events in amorphous silicon, where the activation energy for the forward relaxation is higher than that for the reverse one [51,52]. Furthermore, due to the limited time scale of the MD simulations, atomic relaxation events with higher activation energies may not be fully captured. Consequently, this difference in the sampled relaxation events contributes to the discrepancy in activation energy between the MD simulations and internal-friction experiments. Additionally, the discrepancy may reflect the limited transferability of the empirical potential used in this study. Accordingly, despite the difference in activation energy, we can conclude that the experimentally observed atomic relaxation is caused by reversible atomic shuffling events that act as precursors to the ω and α'' martensitic transformations.

The activation energies associated with the atomic shuffling events that lead to embryonic ω or nanodomain structures are relatively low; consequently, such shuffling can occur even at low temperatures. Because these shuffling events do not involve significant volumetric strain, they are not accompanied by a substantial increase in elastic strain energy, which would otherwise raise the activation barrier. In addition to volumetric strain effects, the activation energy is also expected to correlate with the shuffling amplitude, a relationship that should be quantified in future work.

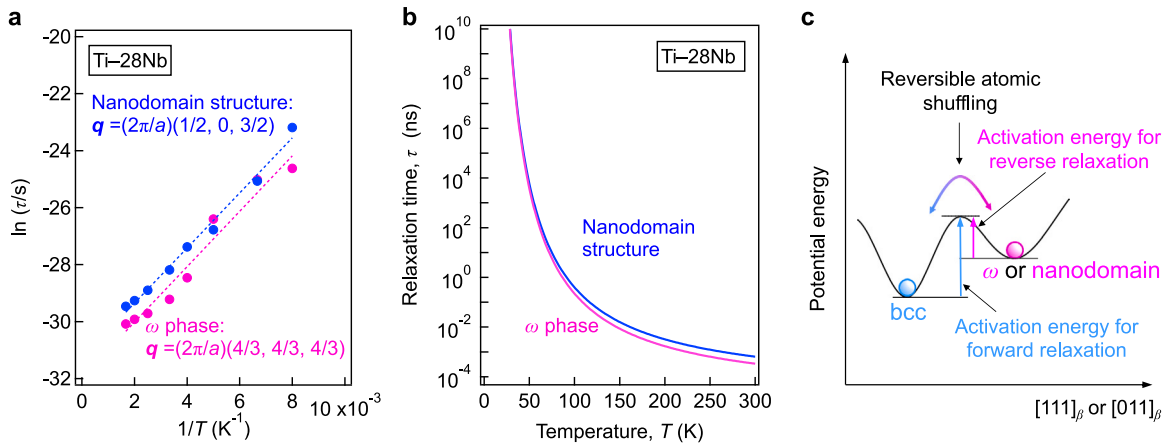

Fig. 9. Thermal activation of pretransitional, reversible atomic shuffling events. (a) Arrhenius plots of the relaxation time τ for the intermediate scattering function $F(\boldsymbol{q},t)$ in Ti–28Nb. The plots correspond to the relaxation from the ω phase ($\boldsymbol{q}=(2\pi/a)(4/3,4/3,4/3)$) and the nanodomain structure ($\boldsymbol{q}=(2\pi/a)(1/2,0,3/2)$). (b) Relaxation time τ for the reverse transition (from ω or nanodomain to bcc) in Ti–28Nb. The relaxation times were calculated from the activation energies and pre-exponential factors obtained from the MD simulations. (c) Schematic explaining reversible atomic shuffling events and the corresponding activation energies for the forward (from bcc (β) to ω or nanodomain) and reverse relaxations.

4. Discussion

The relaxation times τ for the reverse transitions (from ω or nanodomain to bcc) for the Ti–28Nb alloy were calculated from the activation energies and pre-exponential factors which were obtained from the MD simulations. The τ values increased with a decrease in the temperature (Fig. 9(b)). Below ~90 K, the τ values were greater than 1 ns, which is the averaging window used for computing the elastic-stiffness tensor. Thus, within the simulation window considered in this study, atomic relaxation rarely occurs at temperatures below ~90 K; that is, the relaxation is effectively frozen on the simulation time scale. A decrease in the relaxation frequency at low temperatures resulted in a decrease in the stress-fluctuation frequency, thereby leading to a sharp increase in the elastic moduli below ~100 K (Fig. 4(a) and 4(b)). These increases correspond to the ΔM effect observed in the experimentally measured Young's modulus (Fig. 3(a)), wherein the atomic-relaxation-freeze temperature depends on the ensemble-averaging time, analogous to elastic-modulus measurements at different resonance frequencies. We therefore conclude that elastic-stiffness calculations based on the stress-fluctuation formula are effective for evaluating the effect of anelastic relaxation on the elastic properties, and that anelastic relaxation lowers the elastic moduli of Ti–Nb alloys.

In regions wherein the bcc phase is locally less stable due to the statistical compositional fluctuations, the softening of the transverse-acoustic $TA(1/2)(1,1,0)$ and longitudinal-acoustic $LA(2/3)(1,1,1)$ phonon modes probably lowers the energy barrier for the atomic shuffling involved in the α'' martensitic and ω transformations. This effect can be attributed to the fact that phonon softening decreases the curvature of the atomic potential-energy surface. Consequently, in Nb-lean, less-stable bcc regions, the formation of the embryonic state due to atomic shuffling and its subsequent reversion to the bcc state cycle repeatedly when phase nucleation is suppressed by a high energy barrier (Fig. 9(c)). The reversible atomic shuffling events lead to significant anelastic relaxation that leads to a decrease in the shear moduli c' and c_{44}, even at room temperature (~300 K). This mechanism clarifies the ultimate decreases in c' and c_{44} due to softening of short-wavelength phonons. The magnitude of the anelastic-relaxation-induced reductions in c' and c_{44} increases with a decrease in the Nb concentration in Ti–Nb alloys because shuffling is localized to Nb-lean regions (Supplementary Figs. S4(a), S4(b), S4(d), and S4(e)). Therefore, a low Young's modulus E is obtained in low-stability bcc structures with low concentrations of the bcc-stabilizing element Nb (Supplementary Fig. S5(d)). These findings explain the detailed correlation between a low Young's modulus and low bcc-phase stability.

The nucleation of ω and α'' martensitic phases must be avoided because the formation of these high-modulus phases increases the Young's modulus [18,21]. In contrast, their pretransitional, reversible atomic shuffling events are essential for lowering the Young's modulus, despite their unrecognized significance. Thus, controlling the reversible atomic shuffling events and the resultant anelastic relaxation is an effective strategy for achieving a further decrease in the elastic modulus of biomedical bcc Ti alloys. Crucially, decreasing the activation energy for reversible atomic shuffling and promoting anelastic relaxation are essential to reduce Young's modulus; conversely, increasing the activation energy for the nucleation of ω and α'' martensite phases is necessary to suppress the formation of these high-modulus phases. Accordingly, simultaneously controlling these two activation energies is a key material design strategy for achieving a low Young's modulus. A previous study demonstrated that in Ti–V-based alloys, the addition of Al or oxygen affects quenched-in statistical compositional fluctuations and the activation energy for atomic shuffling [33]. Therefore, adding these ternary or quaternary elements and optimizing the overall composition offer a potential strategy to control reversible atomic shuffling and the resultant anelastic relaxation. Furthermore, the activation energy for the nucleation of ω and α'' phases can be raised by increasing the transformation strain. While the ω transformation is characterized by a small transformation strain, tailoring this strain and increasing the nucleation barrier will also be achieved by adding ternary or quaternary elements and optimizing the alloy composition.

To complement the experimental findings for ternary and quaternary alloys and to enable alloy design and optimization, the current computational framework will be extended beyond binary systems. This involves developing transferable machine-learning interatomic potentials that explicitly consider both substitutional and interstitial alloying elements. These potentials will enable finite-temperature simulations to elucidate the effects of these elements on reversible shuffling and the associated anelastic relaxation.

Heterogeneous polarization fluctuations, known as polar nanoregions (PNRs), develop in the nanoscale regions of $BaTiO_3$-based and other relaxor ferroelectrics [53]. These PNRs are embedded within a matrix that is chemically disordered because of the random distribution of different ions on the crystal lattice. A decrease in the temperature leads to a considerable reduction in the dynamic polarization fluctuations in PNRs and an apparent fluctuation freeze on the experimental

time scale. This freezing process, which occurs below a material- and frequency-dependent freezing temperature, exhibits a non-Arrhenius behavior commonly described by the Vogel–Fulcher relation. Elastic-modulus softening is observed above this freezing temperature. This elastic softening reflects the coupling between the dynamic fluctuations of the PNRs and strain [54]. Although the dynamic fluctuations in the nanoscale regions of relaxor ferroelectrics affect their elastic properties in a manner similar to that in bcc Ti–Nb alloys, the characteristics of these fluctuations and the corresponding regions differ significantly from those in bcc Ti–Nb alloys. To achieve a materials design that reduces the elastic modulus of Ti alloys, the effects of local chemical composition [55] on reversible atomic shuffling events should be clarified in greater detail.

5. Conclusions

We revealed that metastable bcc Ti–Nb alloys exhibit reversible atomic shuffling events that act as precursors to the ω and α'' martensitic transformations. The reversible shuffling has a low average activation energy of 0.20 eV, leading to significant anelastic relaxation even at room temperature (~300 K). The resulting anelastic relaxation reduces the single-crystal shear moduli c' and c_{44}, thereby lowering the polycrystalline Young's modulus. The reversible atomic shuffling events occur in the sub-nanometer low-stability bcc regions that are statistically depleted in the bcc-stabilizing element, Nb. The local Nb concentration within the second-nearest-neighbor (2NN) shell in these regions is the primary factor governing the magnitude of atomic relaxation. Thus, controlling the reversible atomic shuffling events by manipulating the quenched-in statistical compositional fluctuations and the resultant local chemical composition is an effective strategy for designing biomedical bcc Ti alloys with an elastic modulus lower than that of conventional biomaterials. To achieve this materials design, the effects of local chemical composition on the reversible atomic shuffling events should be clarified in greater detail.

CRediT authorship contribution statement

Masakazu Tane: Writing – review & editing, Writing – original draft, Visualization, Validation, Supervision, Software, Resources, Project administration, Methodology, Investigation, Funding acquisition, Formal analysis, Data curation, Conceptualization. **Keigo Morita:** Investigation. **Eisuke Miyoshi:** Validation, Software, Investigation. **Takumi Hiramatsu:** Investigation.

Declaration of competing interest

The authors declare that they have no known competing financial interests or personal relationships that could have appeared to influence the work reported in this paper.

Acknowledgments

This work was supported by JST PRESTO [Grant Number JPMJPR1996], JSPS KAKENHI [Grant Number 21H01653, 24K01201, and 25K22170], and a research grant from the Light Metal Educational Foundation [Grant Number 2025-A-014].

Appendix A. Supplementary materials

Supplementary material related to this article can be found online at https://doi.org/10.1016/j.actamat.2026.121969.

Data availability

Data will be made available on request.

References

[1] D. Banerjee, J.C. Williams, Perspectives on titanium science and technology, Acta Mater. 61 (2013) 844–879.
[2] M. Long, H.J. Rack, Titanium alloys in total joint replacement - a materials science perspective, Biomaterials 19 (1998) 1621–1639.
[3] Y. Tian, L. Zhang, D. Wu, R. Xue, Z. Deng, T. Zhang, L. Liu, Achieving stable ultra-low elastic modulus in near-β titanium alloys through cold rolling and pre-strain, Acta Mater. 286 (2025) 120726.
[4] B. Yu, N. Ding, H. Chen, X. Yang, H. Wang, J. Chen, Z. Cai, G. Xie, Design strategy of Ti-Zr-Hf-Nb high-entropy alloys based on first principles computations, Acta Mater. 295 (2025) 121183.
[5] Y.L. Hao, S.J. Li, S.Y. Sun, C.Y. Zheng, R. Yang, Elastic deformation behaviour of Ti-24Nb-4Zr-7.9Sn for biomedical applications, Acta Biomater. 3 (2007) 277–286.
[6] P. Laheurte, F. Prima, A. Eberhardt, T. Gloriant, M. Wary, E. Patoor, Mechanical properties of low modulus β titanium alloys designed from the electronic approach, J. Mech. Behav. Biomed. Mater. 3 (2010) 565–573.
[7] K. Hinoshita M. Abdel-Hady, M. Morinaga, General approach to phase stability and elastic properties of β-type Ti-alloys using electronic parameters, Scr. Mater. 55 (2006) 477–480.
[8] V.J. Challis, X. Xu, A. Halfpenny, A.D. Cramer, M. Saunders, A.P. Roberts, T.B. Sercombe, Understanding the effect of microstructural texture on the anisotropic elastic properties of selective laser melted Ti-24Nb-4Zr-8Sn, Acta Mater. 254 (2023) 119021.
[9] E. Alabort, Y.T. Tang, D. Barba, R.C. Reed, Alloys-by-design: A low-modulus titanium alloy for additively manufactured biomedical implants, Acta Mater. 229 (2022) 117749.
[10] M.P. Staiger, A.M. Pietak, J. Huadmai, G. Dias, Magnesium and its alloys as orthopedic biomaterials: A review, Biomaterials 27 (2006) 1728–1734.
[11] R. Kondo, N. Nomura, Y. Tsutsumi Suyalatu, H. Doi, T. Hanawa, Microstructure and mechanical properties of as-cast Zr–Nb alloys, Acta Biomater. 7 (2011) 4278–4284.
[12] R. Xue, D. Wang, Y. Tian, J. Wang, L. Liu, L. Zhang, Zr–xNb–4Sn alloys with low Young's modulus and magnetic susceptibility for biomedical implants, Prog. Nat. Sci. Mater. Int. 31 (2021) 772–778.
[13] R. Salloom, S.A. Mantri, R. Banerjee, S.G. Srinivasan, First principles computation of composition dependent elastic constants of omega in titanium alloys: implications on mechanical behavior, Sci. Rep. 11 (2021) 12005.
[14] J. Sun, Q. Yao, H. Xing, W.Y. Guo, Elastic properties of β, α'' and ω metastable phases in Ti–Nb alloy from first-principles, J. Phys. : Condens. Matter 19 (2007) 486215.
[15] K.M. Kim, H.Y. Kim, S. Miyazaki, Effect of Zr content on phase stability, deformation behavior, and Young's modulus in Ti-Nb-Zr alloys, Materials 13 (2020) 476.
[16] X. Zhao, M. Niinomi, M. Nakai, J. Hieda, T. Ishimoto, T. Nakano, Optimization of Cr content of metastable β-type Ti–Cr alloys with changeable Young's modulus for spinal fixation applications, Acta Biomater. 8 (2012) 2392–2400.
[17] H. Ikehata, N. Nagasako, T. Furuta, A. Fukumoto, K. Miwa, T. Saito, First-principles calculations for development of low elastic modulus Ti alloys, Phys. Rev. B 70 (2004) 174113.
[18] M. Tane, S. Akita, T. Nakano, K. Hagihara, Y. Umakoshi, M. Niinomi, H. Nakajima, Peculiar elastic behavior of Ti–Nb–Ta–Zr single crystals, Acta Mater. 56 (2008) 2856–2863.
[19] J.H. Dai, Y. Song, W. Li, R. Yang, L. Vitos, Inffluence of alloying elements Nb, Zr, Sn, and oxygen on structural stability and elastic properties of the Ti2448 alloy, Phys. Rev. B 89 (2014) 014103.
[20] P. Lazar, M. Jahnatek, J. Hafner, N. Nagasako, R. Asahi, M. Stohr C. Blaas-Schenner, R. Podloucky, Temperature-induced martensitic phase transitions in gum-metal approximants: First-principles investigations for Ti_3Nb, Phys. Rev. B 84 (2011) 054202.
[21] M. Tane, S. Akita, T. Nakano, K. Hagihara, Y. Umakoshi, M. Niinomi, H. Mori, H. Nakajima, Low Young's modulus of Ti–Nb–Ta–Zr alloys caused by softening in shear moduli c' and c_{44} near lower limit of body-centered cubic phase stability, Acta Mater. 58 (2010) 6790–6798.
[22] H.W. Jeong, Y.S. Yoo, Y.T. Lee, J.K. Park, Elastic softening behavior of Ti–Nb single crystal near martensitic transformation temperature, J. Appl. Phys. 108 (2010) 063515.
[23] J. Ma R.E. McMahon, S.V. Verkhoturov, I. Karaman D. Munoz-Pinto, F. Rubitschek, H.J. Maier, M.S. Hahn, A comparative study of the cytotoxicity and corrosion resistance of nickel–titanium and titanium–niobium shape memory alloys, Acta Biomater. 8 (2012) 2863–2870.
[24] Y. Bai, Y. Deng, Y. Zheng, Y. Li, R. Zhang, Y. Lv, Q. Zhao, S. Wei, Characterization, corrosion behavior, cellular response and in vivo bone tissue compatibility of titanium–niobium alloy with low Young's modulus, Mater. Sci. Eng. C 59 (2016) 565–576.
[25] H. Matsumoto, S. Watanabe, S. Hanada, Beta TiNbSn alloys with low Young's modulus and high strength, Mater. Trans. 46 (2005) 1070–1078.
[26] S.K. Sikka, Y.K. Vohra, R. Chidambaram, Omega phase in materials, Prog. Mater. Sci. 27 (1982) 245–310.

[27] W. Petry, A. Heiming, J. Trampenau, M. Alba, C. Herzig, H.R. Schober, G. Vogl, Phonon dispersion of the bccphase of group-IV metals. I. bcc titanium, Phys. Rev. B 43 (1991) 10933–10947.
[28] K. Otsuka, X. Ren, Physical metallurgy of Ti–Ni-based shape memory alloys, Prog. Mater. Sci. 50 (2005) 511–678.
[29] X. Moya, L. Manosa D. Gonzalez-Alonso, A. Planes, V.O. Garlea, T.A. Lograsso, D.L. Schlagel, J.L. Zarestky, S. Aksoy, M. Acet, Lattice dynamics in magnetic superelastic Ni-Mn-In alloys: Neutron scattering and ultrasonic experiments, Phys. Rev. B 79 (2009) 214118.
[30] A. Zheludev, S.M. Shapiro, P. Wochner, A. Schwartz, M. Wall, L.E. Tanner, Phonon anomaly, central peak, and microstructures in Ni_2MnGa, Phys. Rev. B 51 (1995) 11310–11314.
[31] S.M. Shapiro, B.X. Yang, G. Shirane, Y. Noda, L.E. Tanner, Neutron scattering study of the martensitic transformation in a Ni-Al β-phase alloy, Phys. Rev. Lett. 62 (1989) 1298–1301.
[32] M. Tane, H. Nishiyama, A. Umeda, N.L. Okamoto, K. Inoue, M. Luckabauer, Y. Nagai, T. Sekino, T. Nakano, T. Ichitsubo, Diffusionless isothermal omega transformation in titanium alloys driven by quenched-in compositional fluctuations, Phys. Rev. Mater. 3 (2019) 043604.
[33] M. Tane, H. Nishio, D. Egusa, T. Sasaki, E. Abe, E. Miyoshi, S. Higashino, Effects of aluminum and oxygen additions on quenched-in compositional fluctuations, dynamic atomic shuffling, and their resultant diffusionless isothermal ω transformation in ternary Ti–V-based alloys with bcc structure, Acta Mater. 255 (2023) 119034.
[34] N.L. Okamoto, S. Kasatani, M. Luckabauer, R. Enzinger, S. Tsutsui, M. Tane, T. Ichitsubo, Evolution of microstructure and variations in mechanical properties accompanied with diffusionless isothermal ω transformation in β-titanium alloys, Phys. Rev. Mater. 4 (2020) 123603.
[35] L. Landau, E. Lifshitz, Statistical Physics: V. 5: Course of Theoretical Physics, Pergamon Press, Oxford, 1968.
[36] R.C. Ehemann, J.W. Wilkins, Force-matched empirical potential for martensitic transitions and plastic deformation in Ti-Nb alloys, Phys. Rev. B 96 (2017) 184105.
[37] K. Momma, F. Izumi, VESTA 3 for three-dimensional visualization of crystal, volumetric and morphology data, J. Appl. Crystallogr. 44 (2011) 1272–1276.
[38] M. Tahara, H.Y. Kim, T. Inamura, H. Hosoda, S. Miyazaki, Lattice modulation and superelasticity in oxygen-added β-Ti alloys, Acta Mater. 59 (2011) 6208–6218.
[39] Y. Zheng, R.E. A. Williams, S. Nag, R. Banerjee, H.L. Fraser, D. Banerjee, The effect of alloy composition on instabilities in the β phase of titanium alloys, Scr. Mater. 116 (2016) 49–52.
[40] N.L. Okamoto, S. Kasatani, M. Luckabauer, M. Tane, T. Ichitsubo, Effects of solute oxygen on kinetics of diffusionless isothermal ω transformation in β-titanium alloys, Scr. Mater. 188 (2020) 88–91.
[41] M. Hirao, H. Ogi, EMATs for Science and Industry: Noncontacting Ultrasonic Measurements, Kluwer Academic Publishers, Dordrecht, 2013.
[42] A.P. Thompson, H.M. Aktulga, R. Berger, D.S. Bolintineanu, W.M. Brown, P.S. Crozier, P.J. in't Veld, A. Kohlmeyer, S.G. Moore, T.D. Nguyen, R. Shan, M.J. Stevens, J. Tranchida, C. Trott, S.J. Plimpton, LAMMPS - a flexible simulation tool for particle-based materials modeling at the atomic, meso, and continuum scales, Comput. Phys. Comm. 271 (2022) 108171.
[43] A. van de Walle, M. Asta, G. Ceder, The alloy theoretic automated toolkit: A user guide, Calphad 26 (2002) 539–553.
[44] J.R. Ray, A. Rahman, Statistical ensembles and molecular dynamics studies of anisotropic solids, J. Chem. Phys. 80 (1984) 4423–4428.
[45] G. Gao, K. Van Workum, J. David Schall, J.A. Harrison, Elastic constants of diamond from molecular dynamics simulations, J. Phys. : Condens. Matter 18 (2006) S1737.
[46] R. Hill, The elastic behaviour of a crystalline aggregate, Proc. Phys. Soc. A 65 (1952) 349–354.
[47] A. Nowick, B. Berry, Anelastic Relaxation in Crystalline Solids, Academic Press, New York, 1972.
[48] B.S. Berry, W.C. Pritchet, Computer modeling of relaxation peaks involving a Gaussian distribution of activation energies, Physica Status Solidi (B) 144 (1987) 375–384.
[49] M. Bonisch, M. Calin, L. Giebeler, A. Helth, A. Gebert, W. Skrotzki, J. Eckert, Composition-dependent magnitude of atomic shuffles in Ti–Nb martensites, J. Appl. Crystallogr. 47 (2014) 1374–1379.
[50] W. Sinkler, D.E. Luzzi, The diffuse ω structure: its relationship to spontaneous vitrification in β-Ti–Cr, J. Alloys Compd. 194 (1993) 273–278.
[51] H. Kallel, N. Mousseau, F. Schiettekatte, Evolution of the potential-energy surface of amorphous silicon, Phys. Rev. Lett. 105 (2010) 045503.
[52] N. Mousseau, G.T. Barkema, Activated mechanisms in amorphous silicon: An activation-relaxation-technique study, Phys. Rev. B 61 (2000) 1898–1906.
[53] H. Liu, X. Shi, Y. Yao, H. Luo, Q. Li, H. Huang, H. Qi, Y. Zhang, Y. Ren, S.D. Kelly, K. Roleder, J.C. Neuefeind, L.-Q. Chen, X. Xing, J. Chen, Emergence of high piezoelectricity from competing local polar order–disorder in relaxor ferroelectrics, Nat. Commun. 14 (2023) 1007.
[54] F. Cordero, F. Trequattrini, M. Venet P.S. da Silva, O. Aktas, E.K.H. Salje, Elastic precursor effects during $Ba_{1-x}Sr_xTiO_3$ ferroelastic phase transitions, Phys. Rev. Res. 5 (2023) 013121.
[55] Z. Li, H. Li, L. Zhao, H. Zong, X. Ding, T. Lookman, J. Sun, Regulation of athermal ω formation by one-dimensional chemical ordering in Zr-10% Nb alloys, Phys. Rev. Mater. 9 (2025) 083605.